On the Quantitative Analysis of Localized Scattering Centres in Microwave Images

U. Fuchs and H. Wendel

Telefunken System Technik, Dept. VR3E7
Postfach 17 30 D-7900 ULM Germany

ABSTRACT

The paper introduces a new method for quantitatively interpreting microwave images of discrete structures dominated by scattering centres (s.c.). The highly resolved images are produced by means of Microwave Diversity Imaging, MDI; scattering data data collected in the frequency- aspectangle (f, θ) - space are transformed into the twodimensional (x, y) object space. The method transforms the segment of the image, containing a localized s.c. back into the f- θ - domain. Normalizing the results with the result of a unit scatterer yields the spectral scattering behaviour of the 'isolated' s.c.. Comparison of the results with model calculations on the basis of the Geometrical Theory of Diffractions (GTD) allows to relate the s.c. to canonical structures, i.e. to reconstruct at least parts of the object. The method is tested for a simulated scenario of two scatterers. Its superiority over previous exploitation methods is borne out by applying it to experimental and theoretical data on the edge scattering of a metal plate.

INTRODUCTION

The nonlinear inverse problem of (Microwave) Scattering, i.e. the reconstruction of an object off its scattering data is still an unresolved problem. Existing algorithms (Mensa, 1981; Ausherman et al, 1984) e.g. Synthetic Aperture Radar (SAR) or Microwave Divsersity Imaging (MDI), linearise the problem with the Born approximation for dielectric bodies (Boerner, 1980) and the Physical Optics for metallic bodies (Knott, et al, 1985). Spatial object function and spectral scattering data are related via Fourier transformation. In practice, incomplete frequency response scattering data and the coherent nature of the microwaves cause difficulties to interpret the images: the image of a discrete structures consists of a few s.c. localized at singular points e.g. glancing points, edges etc. On the other hand, high frequency scattering theories, like the Geometrical Theory of Diffraction (GTD), or its extension the Uniform Geometrical Theory of Diffraction (UTD), predict the scattering behaviour of complex objects by modelling them with simpler (canonical) structures, e.g. straight edges, smooth glancing points a.s.o., with known scattering behaviour.

Quantitative analysis of the s.c. in the microwave images for their frequency, aspect angle and polarization dependence, and comparison of the results wih GTD,UTD- predictions should allow us to identify local geometries of the scattering object; the vistas are open for answering the question as to whether or not an a priori unknown object may be recognized from its microwave image. In a recent publication (Fuchs, at al., 1991), we proposed an exploitation method which processes a series of images with increasing center frequencies (aspect angle) and plots the normalized maximum intensity of s.c. In addition to the high processing effort, this exploitation scheme spoils the high resolution inherent to high resolution imaging: in order to resolve neighboring s.c. the images have to be processed over certain f- θ ranges; since the s.c. are averaged over the same regions. This paper introduces a new method which yields from one image processed in large f- θ - regions, the complete spectral information of all localized s.c. in the image. The method is applied to experimental and theoretical data on the edge scattering of a metal plate.

Section 1 introduces the method in detail and points out the difference to our earlier method. A simulation demonstrates the practical procedure. Section 2 applies the method to experimental images of a metal plate. Section 3 concludes the paper.

1. EXPLOITATION METHOD

The imaging process transforms scattering data collected in **1**. frequency f and aspect angle domains θ into the twodimensional x-y- object space with (Li, at al, 1989)

$$R_{jk}(x, y) = (8/c^2) \int_{f_0} \int_{\theta_0} W_1(f)\, W_2(\theta)(f S_{jk}(f, \theta) \; e^{(j\,4\pi f/c\,(x\cos\theta + y\sin\theta))}\, d\theta\, df \qquad (1)$$

c is the speed of light, θ_0 represents the central aspect angle of the angular integration interval of width $\Delta\theta$, f_0, corresponds to the center frequency of the frequency processing interval of width Δf, and j and k indicate the state of polarization of the receive/transmit antenna. R(x,y) represents a projection of the three dimensional reflectivitiy function of the object onto the x-y-plane (Fig. 1). The target in our experiment was chosen that the off-diagonal elements of [R(x,y)] were identical to zero. The non-vanishing elements corresponded to the situation in which both incoming and scattered waves were polarized either vertically (VV) or horizontally (HH). Henceforth we skip the polarization index. $W_1(f)$, $W_2(\theta)$ are real valued window functions.

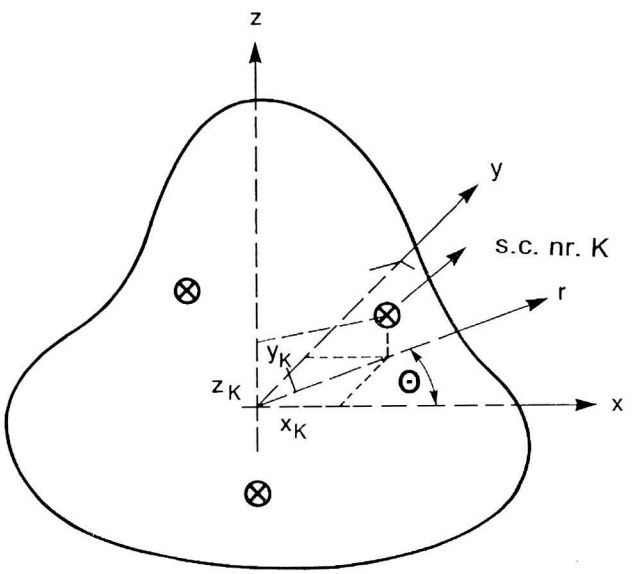

Fig. 1 - Scattering geometry for plane wave incidence (x,y-plane) on an object. The direction of the wave is r. θ is the angle between r and the x axis of the object. ⊗ indicate scattering centres of the object; x_k, y_k, z_k are the coordinates of the k-th scattering centre.

Our original exploitation method takes the relative maximum of the modulus of R(x,y); its position is assumed to coincide with the position $x = x_{max}$, $y = y_{max}$ of a corresponding s.c. whose complex scattering amplitude is given by

$$S(f, \theta) = \left| S(f, \theta) \mid e^{(-j\,4\pi f/c\,(x\cos\theta + y\sin\theta))} \right| \begin{matrix} x = x_{max} \\ y = y_{max} \end{matrix} \qquad (2)$$

We further assumed that the reflectivity associated with this s.c. was given by the value $|R(x, y)|$ assumed for $x = x_{max}$ and $y = y_{max}$, Eqs.(1) and (2) then yield

$$\left| R(x_{max}, y_{max}) \right| = \int_{f_0 - \Delta f/2}^{f_0 + \Delta f/2} \int_{\theta_0 - \Delta\theta/2}^{\theta_0 \Delta\theta/2} W_1(f)\, W_2(\theta) f \mid S(f, \theta) \mid e^{(j\,4\pi f/c\,((x - x_{max})\cos\theta + (y - y_{max})\sin\theta))}\, d\theta\, df \mid \begin{matrix} x = x_{max} \\ y = y_{max} \end{matrix} \qquad (3)$$

In order to get rid of the weighting artifacts, the quantitative discussion of (Fuchs, Wendel, Rvde, 1991) actually employed the normalized reflectivity

$$R^{norm} = \frac{|R(x_{max}, y_{max})|}{\int_{f_0 - \Delta f/2}^{f_0 + \Delta f/2} \int_{\theta_0 - \Delta\theta/2}^{\theta_0 + \Delta\theta/2} f W_1(f)\, W_2(\theta)\, d\theta\, df} \qquad (4)$$

Eqs.(1) and (4) clearly demonstrate: (i) R^{norm} represents a weighted average of the scattering amplitude over finite intervals of frequency and aspect angle.

Our new method uses the linear relationships between the f- θ and the x-y regions: transforming a single s.c. in the image processed in large f- θ regions back into the spectral domains, allows to extract its frequency- and aspect angle dependencies.

We start from the modified reflectivity function, $R^{mod}(x, y)$ defined via ...

$$R^{mod}(x, y) = R(x, y) * rect(2(x_0 - x)/\Delta x) * rect(2(y_0 - y)/\Delta y) \qquad (5)$$

Here, R(x,y) is specified in Eq.(1), and rect $(2z/\Delta z$ is the rectangle function (Lüke, 1985):

$$rect(2z/\Delta z) = \begin{matrix} 1 \text{ if } |2z/\Delta z| \le 1 \\ 0 \text{ if } |2z/\Delta z| \ge 1 \end{matrix} \qquad (6)$$

Thus $R^{mod}(x, y)$ is identical to the measured reflectivity inside an image area of widths Δx and Δy, respectively, centered around (x_o, y_o). Outside this area $R^{mod}(x, y) = 0$.

We then Fourier transform $R^{mod}(x, y)$ into *fcosθ/c – fsinθ/c–space* and at once obtain the complete spectral information on the scattering amplitude, i.e.

$$S^{mod}(f, \theta) = (2\pi)^{-1} \int_{-\infty}^{+\infty} \int_{-\infty}^{+\infty} R^{mod}(x, y)\, e^{(-j\,4\pi f/c\,(x\cos\theta + y\sin\theta))}\, dx\, dy \qquad (7)$$

The size of the transformed image area has to compromise the following: (i) Too small a size causes artifacts in the reconstructed spectrum in terms of additional oscillations. These errors can be very strong if parts of the main peak of the s.c. are eclipsed, and (ii) too big a size risks collecting noise and parts of other s.c. extending into this area. (Fuchs, 1990) shows that the amplitude of the highest error

oscillation in the reconstructed spectrum of a point scatterer is equal to the amplitude of the image function at the eclipsing points ($x = \pm \Delta x/2$, $y = \pm \Delta y/2$). In our experiments, the size of the window was chosen approximately twice the width of the main peak of the Hamming weigthed s.c. This choice amounts to eclipsing the s.c. at its third sidelobe (sidelobe level -43dB) (Harris, 1978). Therefore the error in the reconstructed image is $7*10^{-3} \cong 0.06\,dB$.

In order to correct Eq.(7) for the weighting functions, we divided $S^{mod}(f, \theta)$ by the scattering amplitude of a unit scatterer ($|S_{cal}(f, \theta)| = 1$ manipulated to eqs.(1),(5),(7). Thus in one of our discussions to come we employ the normalized modulus of the scattering amplitude, i.e.

$$S^{norm}(f, \theta) = \left| S^{mod}(f, \theta) \right| / \left| S^{mod}_{cal}(f, \theta) \right| \qquad (8)$$

For our simulation example we assume the scattering amplitude to be given by

$$S(f, \theta) = S_1(f, \theta) + S_2(f, \theta) =$$

$$(f/f_a)^2 * e^{(-j\,4\pi f/c\,(0.075\cos\theta + 0.075\sin\theta))} +$$

$$+ 1 * e^{(-j\,4\pi f/c\,(-0.075\cos\theta - 0.075\sin\theta))} \qquad (9)$$

comprising two s.c., s.c.#1 located at (0.075 m, 0.075 m) with a frequency dependent scattering amplitude, $|S_1|\,(f/f_a)^2$, fa = 8 GHz, and s.c.#2 located at (-0.075 m, -0.075 m) with scattering amplitude $|S_2| = 1$.

Fig. 2 shows the modulus of the scattering amplitude for the frequency range f = 8-18 GHz and the aspect angle range $\Delta\theta = 50°$ with and without Hamming weighting. The imaging algorithm of Eq.1 then yields the image of Fig.3. Following Eq.5 we define the "truncated" reflectivity functions $R^{mod}_{(i)}(x, y)$, i = 1,2: $R^{mod}_{(1)}(x, y) = R(x, y)$ for arguments (x, y) inside the square around s.c. #1 in Fig. 3, $R^{mod}_{(1)}(x, y) = 0$ for all arguments (x, y) outside the square. Similarly $R^{mod}_{(2)}(x, y) = R(x, y)$ for arguments (x, y) inside the square centered at s.c. #2; $R^{mod}_{(2)}(x, y) = 0$ otherwise. Following Eq.7, we next Fourier transform $R^{mod}_{(i)}(x, y)$, i = 1,2, back into $f\cos\theta$–$f\sin\theta$–space, giving rise to the "truncated" scattering amplitude $S^{mod}_{(i)}(x, y)$. Normalization of the result of s.c. #1 to the modulus of the scattering amplitude of s.c. #2 yields the graph of Fig.4a. This ratio actually corresponds to the function Snorm of Eq.8. The spikes at the aperture boundaries are spurious: Both $S^{mod}_{(1)}$ and $S^{mod}_{(2)}$ tend to zero at the aperture boundaries; S^{norm} is ill defined. Fig.4b depicts the logarithm of the amplitude ratio in Cartesian f–θ-coordinates. This Fig. omits the anomalous boundary regions of Fig.4a. S^{norm} does not depend on aspect angle; it depends strongly on frequency. Fig.5 demonstrates this finding more clearly: It extracts the frequency dependence of S^{norm} for $\theta_0 = 30°$ Fig. 4(b) (solid line) and finds the result to agree with the $(f/f_a)^2$ dependence (dashed line) expected from the analytical expression for $|S_1(f, \theta)|$ in Eq.(9).

In the next section we employ the ideas outlined here to actual experimental data obtained by scattering microwaves from a metal plate.

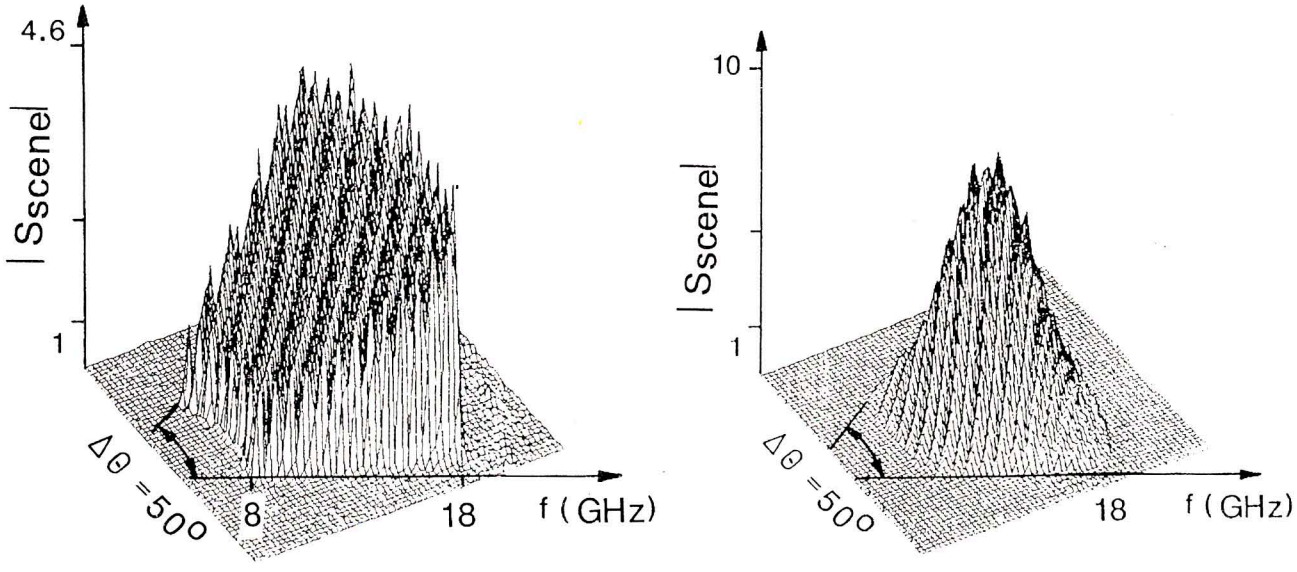

Fig. 2 - Scattering amplitude of the simulation scene of Eq.9 as function of frequency and aspect angle θ. Left: unweighted data. Right: data weighted with Hamming window.

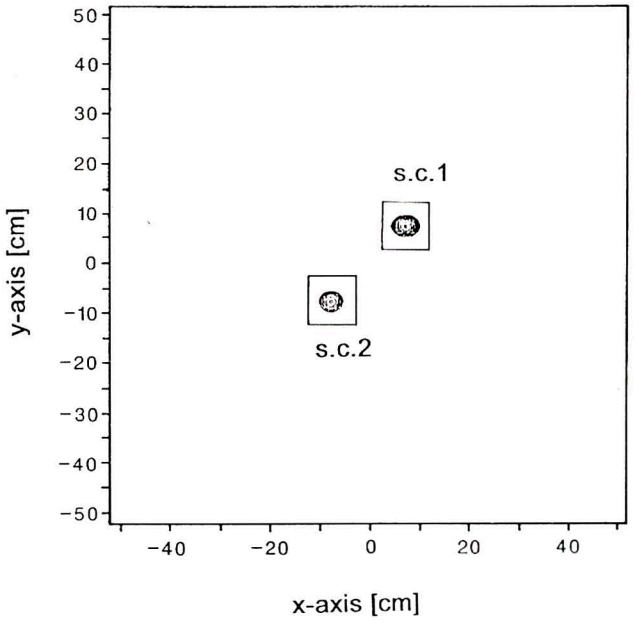

Fig. 3 - Microwave contour image of the simulation scene generated from the scattering amplitude of Eq.9. The image comprises two scattering centres denoted by 1 and 2, respectively. The squares around the sacttering centres indicate the areas which we transformed back into fcos θ -fsin θ -space to yield the spectral representation of Fig.4.

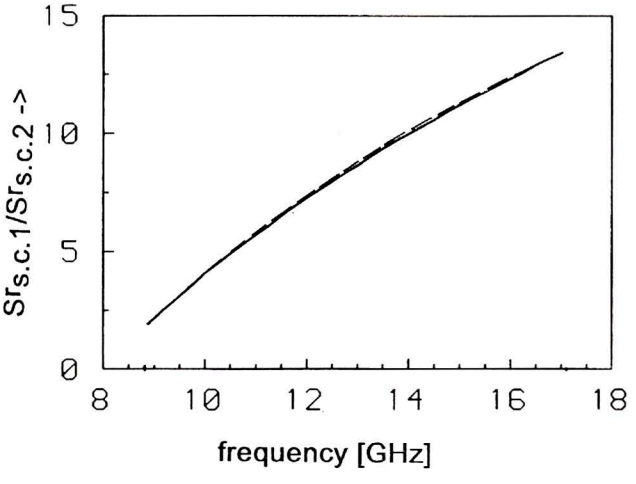

Fig. 5 - Frequency dependence of the ratio of the modulus of the scattering amplitude, $|S_{(1)}^{mod}|$, associated with scattering centre #1 of Fig. 3, and the modulus of the scattering amplitude, $|S_{(2)}^{mod}|$, of scattering centre #2, for θ = 30°. The dashed curve represents the $(f/f_a)^2$ dependence in Eq.9; the solid line derives from Fig. 4b.

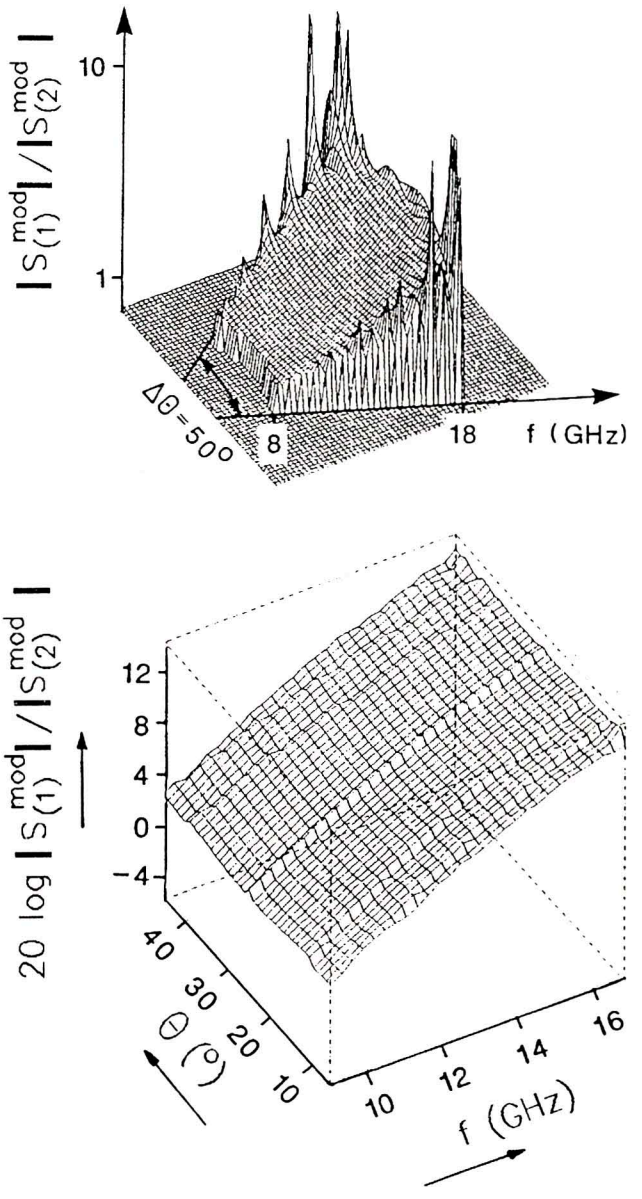

Fig. 4 - Spectral representation of the modulus of the scattering amplitude of scattering centre #1, $|S_{(1)}^{mod}|$, of Fig. 3., divided by the modulus of the scattering amplitude, $|S_{(2)}^{mod}|$, of scattering centre #2. a: Polar representation; b: cartesian representation of 20log ($|S_{(1)}^{mod}|/|S_{(2)}^{mod}|$).

2. EXPERIMENTAL RESULTS

The experiments were carried out with an outdoor range described in detail in (Fuchs, 1990). The measured object a rectangular metal plate with dimensions a=150 mm, height b=300 mm and thickness d=15 mm (Fig. 6a) was rotated on a turntable. We measured the complex amplitude $S(f, \theta)$, i.e. modulus and phase of the backscattered signal in θ– increments of 0.4 degrees at fixed frequency, f. After each complete rotation of the turntable, f was augmented by 100 MHz. Amplitude, phase, frequency and angular position were recorded on computer tape. The polarization of the transmit/receive antenna was chosen to be H-H. We processed images of the geometry in Fig.6a for the two centre aspect angles $\theta_0 = 27.5°$, 62.5° and for $f_0 = 13.5$ GHz, $\Delta f = 10$ GHz and $\Delta\theta = 45°$. Fig. 6b shows the image for $\theta_0 = 62.5°$, consisting of two s.c. at the visible near (n) and far (f) plate ends. The measurement did not resolve the two near end plate edges 1.5 cm apart; thus in Fig. 6b the n-s.c. appears broadenend in comparison with the f- s.c. Next we transformed the squared regions (cf. Fig. 6b) around the n- and f- s.c. back into the f-θ regions. Fig. 7 shows the results for the n- centre and Fig. 8 the results for the f- centre after the scattering intensities were normalized to the backscatter intensity recorded for perpendicular wave incidence. We see: (i) Back transformation immediately yields the combined frequency/aspect angle dependence of the mechanisms involved in the near and far end scattering. Generating diagrams of the kind of Fig. 7,8 with the old exploitation method would mean to process at least 56 images (8 center frequencies shifted by 1 GHz between 9.5-16.5 GHz and 7 center aspect angles shifted by 10° between 20 ° - 70°). Even then the scattering amplitudes are averaged over considerable bandwidth in frequency ($\Delta f = 3$ GHz and aspect angle ($\Delta\theta = 30°$) which tends to hide the sensitivity in the scattering diagrams of the s.c.; (ii) the overall behaviour of the edges as for frequency and aspect angle dependence of the mechanisms involved is quite different. The diagram of the far end varies smoothly with aspectangle, in the range $\theta = 10 - 45°$ and for increasing frequencies, it oscillates in the region $\theta = 45 - 80°$. The scattering behaviour of the near end edges is much more spectacular: a valley crosses the two diagrams reminding of destructive interference between the near end edges. For this reason a simple GTD simulation modelled the far end plate with one isolated rectangular edge and the near end plate with two interfering isolated rect. edges

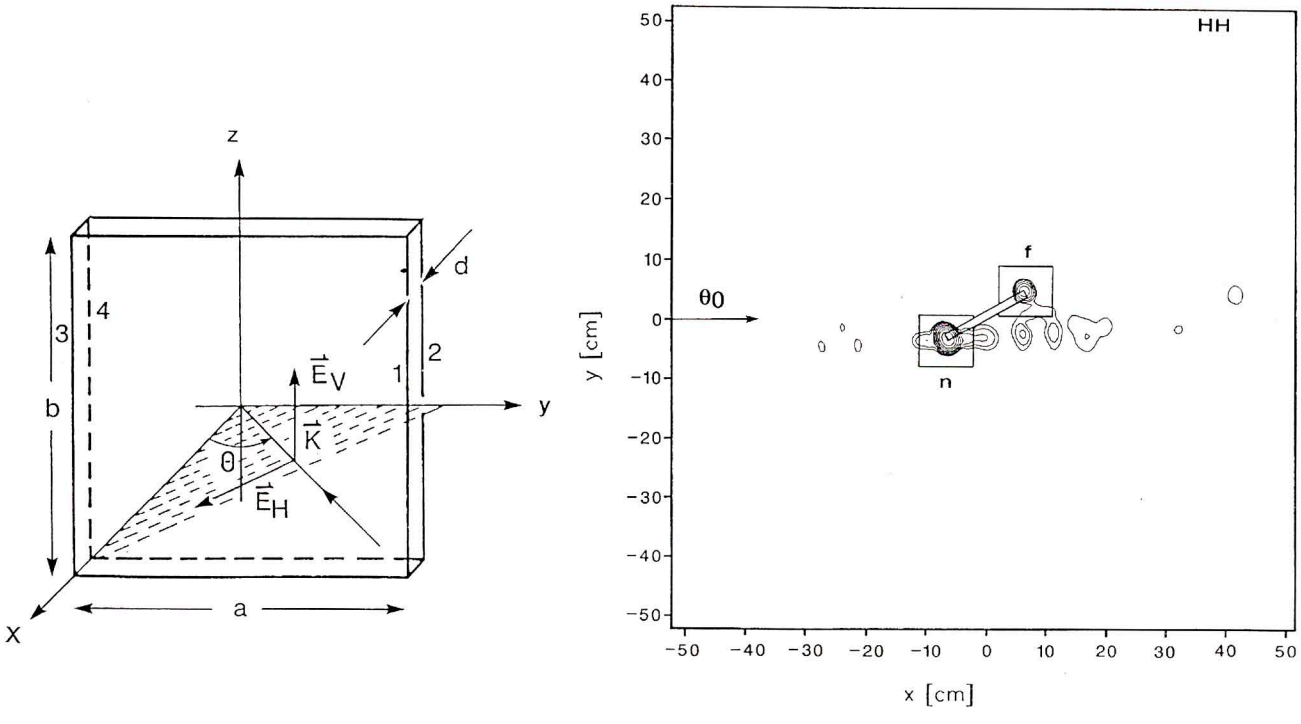

Fig. 6 - Scattering geometry (a) and microwave contour image (b) of the metal plate employed in our measurement. The dimensions were: a=15cm, b=30cm, d=1.5cm. The plane of wave incidence was the x-y-plane. The electric vector of the polarized wave was perpendicular to the z-axis and to the direction of the wave vector. The aspect angle, θ, was counted from the x-axis. The image was processed from experimental data for θ = 85° . θ_0 is the central aspect angle of the processing interval. Transmit/receive polarizations were horizontal. "n" denotes the two plate edges closest to the radar, "f" denotes the plate edge more distant, (cf Fig. 14.). Neighboring contour lines differ by 3dB in intensity. The squares around the s.c. indicate the segments employed in the backtransformation.

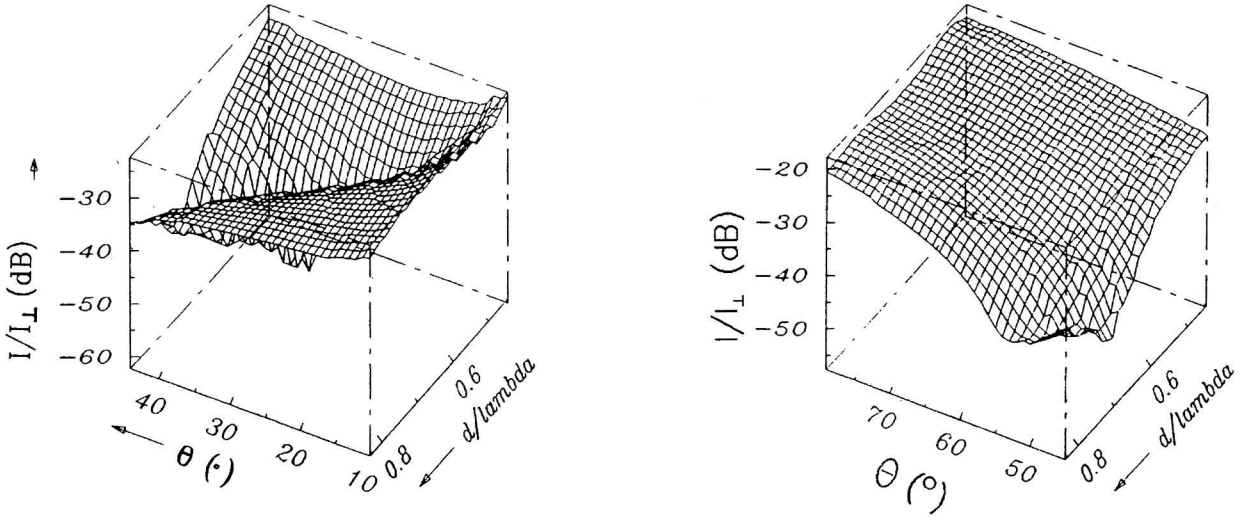

Fig. 7 - "Frequency"-aspect angle spectra after backtransforming n-scattering centre. The spectrum is normalized to the intensity for perpendicular wave incidence, I Instead of frequency we chose the ratio d/λ which is proportional to frequency; d is the thickness of the metal plate, λ is the wavelength of the microwave. (a) covers the θ- regime between 10 ° and 45 ° and (b) the θ- between 45 ° and 85 °. d/λ variies between 0.45 and 0.85.

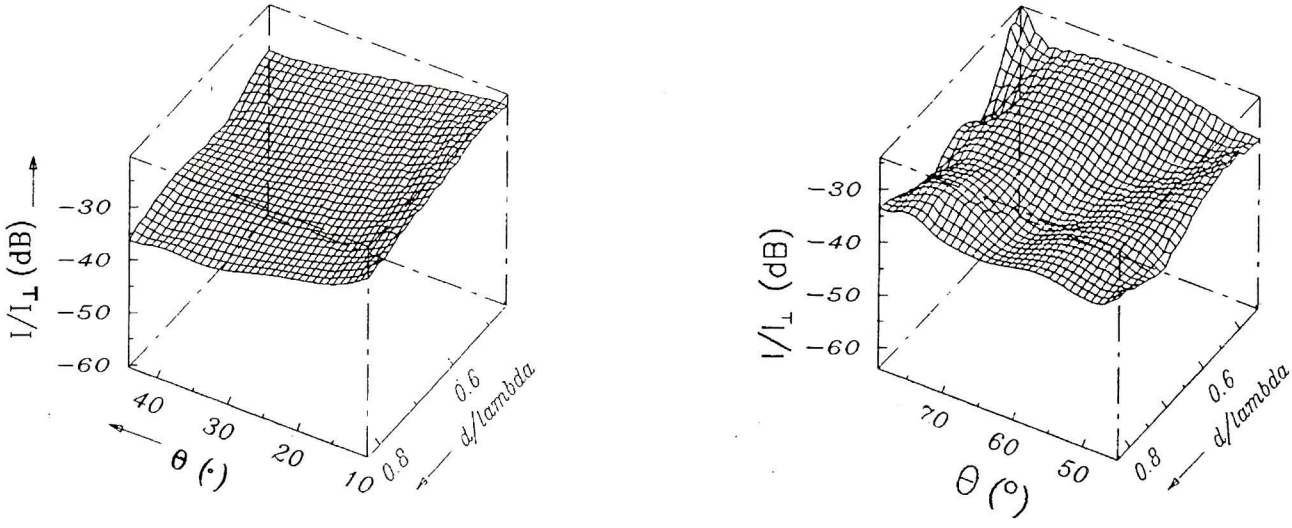

Fig. 8 - "Frequency"- aspect angle spectra after backtransforming f-scattering centre. The representation is the same as in Fig. 7. (a) covers the θ- regime between 10 ° and 45 ° and (b) the θ- regime between 45 ° and 85 °. d/λ variies between 0.45 and 0.85.

(cf. Eq's A3,A6.). Fig. 9 gives the results of the n-edges and Fig.10 those of the f-edges in the same representation as Fig.7,8: for both plate ends, n and f, the diagrams reflect the overall scattering behaviour found in the experiments. For a more detailed analysis we have plotted the differences between theoretical and experimental results for the n-s.c. in Fig.11 and for the f-s.c. in Fig.12. The simple simulation cannot explain the oscillation in the scattering diagram of the f-s.c (Fig. 8), it also overestimates the break-in in the diagrams of the n-s.c: we could improve the correspondence between theory and eperiment by adding second order wave propagation between the three visible edges. For a more detailed discussion, we refer to (Fuchs, 1990).

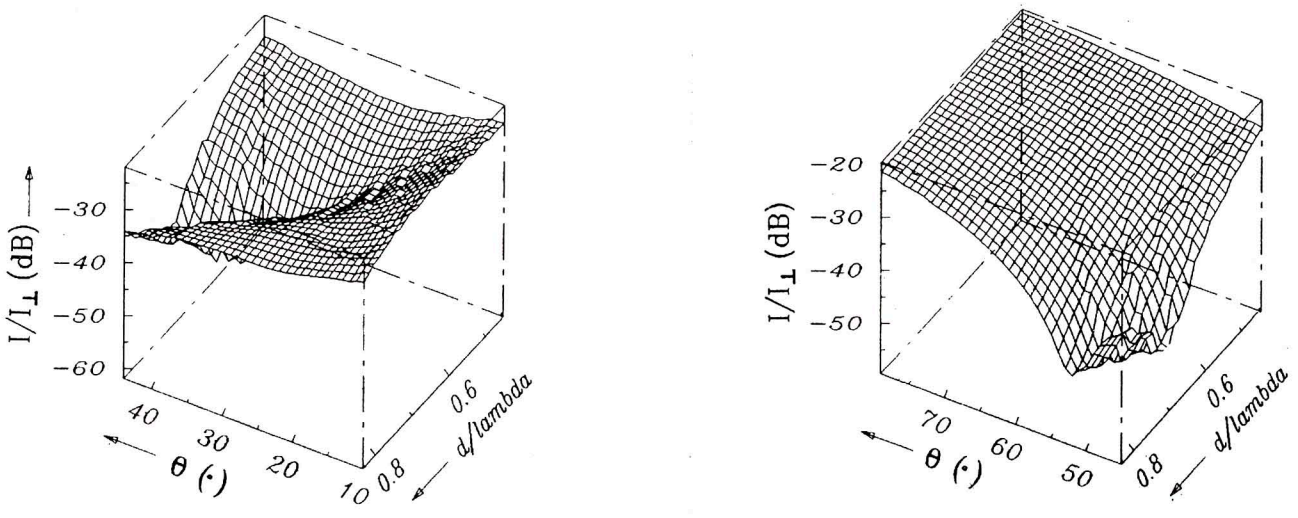

Fig. 9 - "Frequency"-aspect angle spectra of the GTD simulation of the n-scattering centre. The representation is the same as in Fig.7. (a) covers the θ- regime between 10 ° and 45 ° and (b) the θ- regime between 45 ° and 85 °. d/λ variies between 0.45 and 0.85.

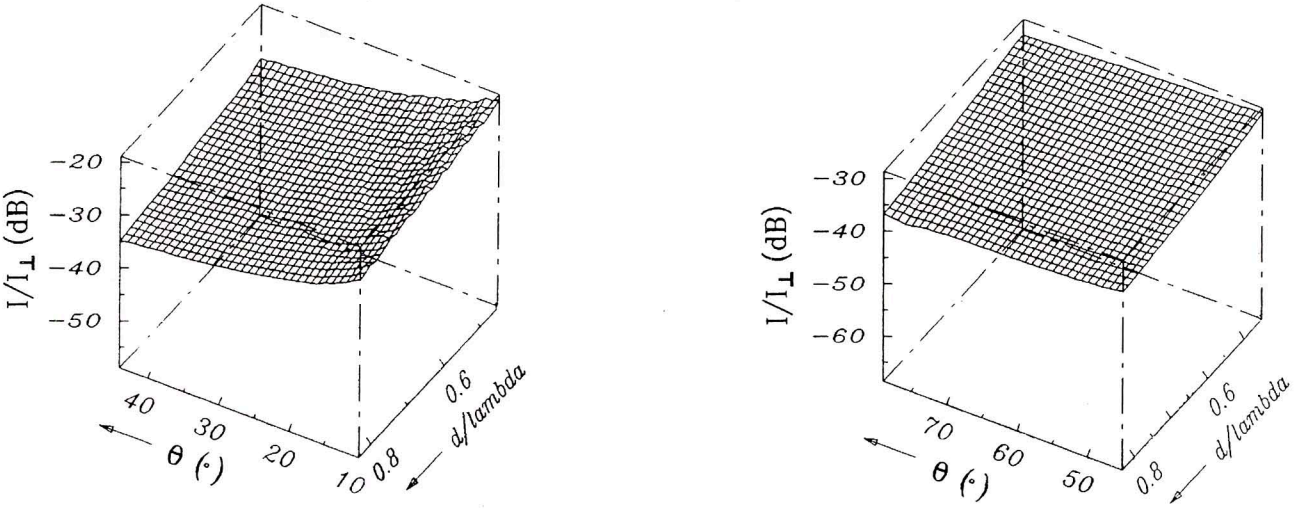

Fig. 10 - "Frequency"-aspect angle spectra of the GTD simulation of the f-scattering centre. The representation is the same as in Fig.7. (a) covers the θ- regime between 10 ° and 45 ° and (b) the θ- regime between 45 ° and 85 °. d/λ varies between 0.45 and 0.85.

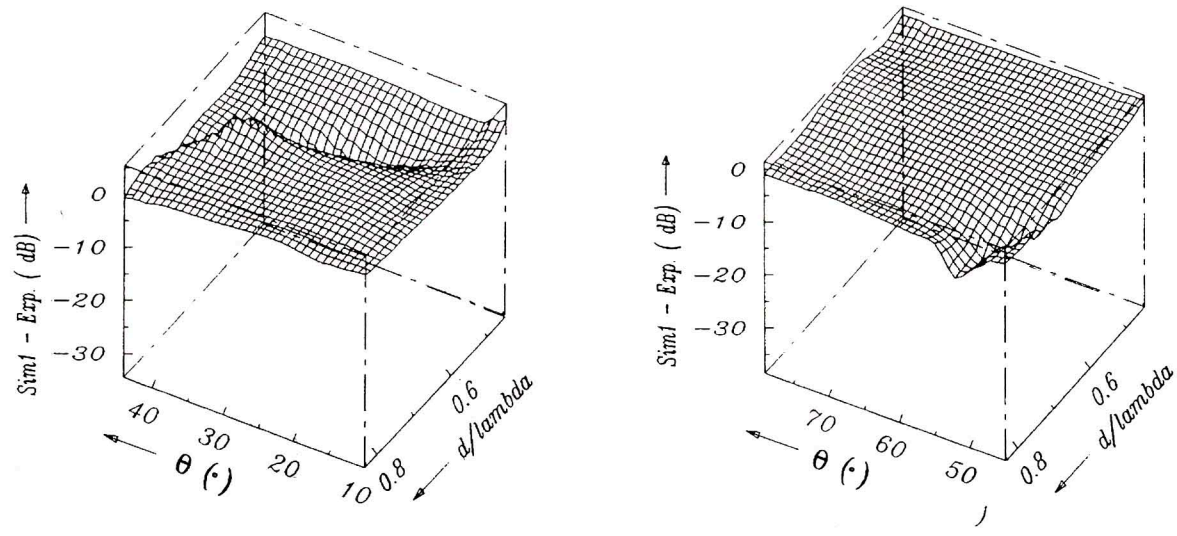

Fig. 11 - n- scattering centre: Difference between experiment in Fig. 7 and simulation in Fig. 9.

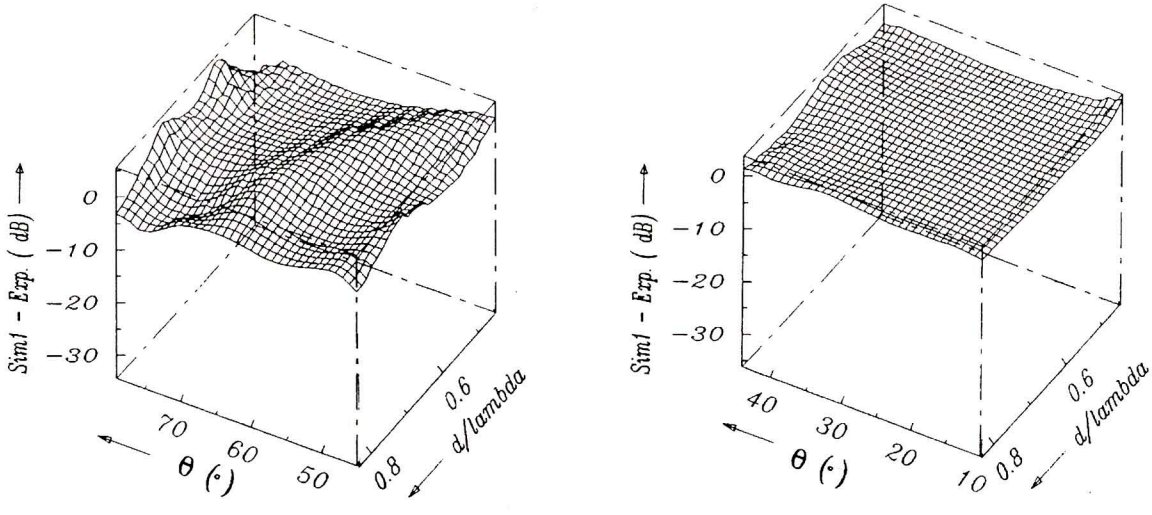

Fig. 12 - f-scattering centre: Difference between experiment in Fig.8 and simulation in Fig.10.

CONCLUSION

This paper introduced a new method for quantitatively analyzing microwave images of discrete structures. The method extracts the complete spectral information of the localized scattering centres, e.g. aspect angle and frequency, hidden in a single image. The method relied on the backtransformation of isolated parts of the image which comprises local scattering centres. After laying the theoretical basis the method was tested for a simulated scenario of two s.c. The experimental verification for the edge scattering of a metal plate showed: (i) The scattering behaviour of the s.c. localized at the near (n) and far (f) visible plate ends differ qualitatively and quantitatively; and (ii) the f-s.c. could be explained as the scattering of an isolated rectangular edge, corresponding to the visible edge of the far plate end. The n-s.c. was identified as the combined scattering of the two neighboring edges forming the near plate end. Altogether the experimental results of the metal plate confirmed the concept proposed in this paper: quantitative analysis of s.c. in the images with the proposed exploitation method and comparison of the results with theoretically derived scattering diagrams of canoncial structures, allowed us to extract local geometries.

ACKNOWLEDGEMENTS

The imaging experiments on the metal plate were carried out by one of the authors (U.F.), on the radar outdoor range of the DLR, Oberpfaffenhofen, Germany.

REFERENCES

Mensa D.L., 1981, High Resolution Radar Imaging. (Washington: Artech House).

Ausherman D.A. and Kozma A. and Walker J.L. and Harrison M.J. and Poggio E.C., 1984, Developements in Radar Imaging. IEEE Trans. on AES, Vol.20.

Boerner W.M., 1980, Polarization Utilization in Electromagnetic Inverse Scattering in 'Scattering Problems in Optics' (Berlin, Heidelberg, New York: Springer Verlag).

Knott E.F. and Schaeffer J.S. and Tuley M.T., 1985, Radar Cross Section (Norwood, Massachusetts: Artech House).

Fuchs U. and Wendel H. and Rvde B., 1991, On the Frequency and Polarization Dependence of 2D Microwave Edge Diffraction. AE\45(5), 313.

Li H.J. and Farhat N.H. and Shen Y. and Werner C.L., 1989, Image Understanding and Interpretation in Microwave Diversity Imaging. IEEE AES 37, 1048.

Lüke H.D., 1985, Signalübertragung (Berlin: Springer Verlag).

Fuchs U., 1990, Streuzentrenanalyse in der Mikrowellenabbildung einfacher metallischer Streukvrper. DLR-FB 90-32.

Harris F.J., 1978, On the Use of Windows for Harmonic Analysis with the Discrete Fourier Transform, Proc. of IEEE 66, 51.

Keller J.B., 1962, Geometrical Theory of Diffraction, J. Opt. Soc. America 52, 116.

Hansen R.C., 1981, Geometric Theory of Diffraction (New York: IEEE Press).

Pathak P.H., 1974, An Uniform Geometrical Theory of Diffraction for an Edge in a Perfectly Conducting Surface, Proc. of IEEE 62, 1448.

Ross R.A., 1966, Radar Cross Section of Rectangular Flat Plates as a Function of Aspect Angle, IEE Trans. AP-14, 329.

Appendix A. Computation of the backscattering of a cuboid with the methods of the GTD/UTD

For the scattering geometry of Fig. 6, the main scattering contributions originate from the edges perpendicular to the radar line of sight. The scattered rays are orientated in a plane perpendicular to the edges. Parts of them are backscattered to the radar (single diffracted rays), parts of them hit neighbouring edges and produce multiple diffracted rays. If a plane or cylindrical wave u^{i_H} with polarization H hits an edge (cf. Fig. 13) the scalar diffracted field u^{d_H} is (Keller, 1962; Hansen, 1981; Pathak, 1974):

$$u_H^d = u_H^i \, 1/\sqrt{s} \, D_{eH}(\Phi, \Phi', kL) \tag{A.1}$$

D_{eH} is given by

$$\begin{aligned} D_{eH}(\Phi, \Phi', kL) = & - e^{(-j\pi/4)}/(6\pi\sqrt{f/c}) * \\ & \Bigg\{ \cot\frac{\pi + (\Phi - \Phi')}{2\eta} * F(kLa^+(\Phi - \Phi')) + \\ & \cot\frac{\pi - (\Phi - \Phi')}{2\eta} * F(kLa^-(\Phi - \Phi')) + \\ & \cot\frac{\pi + (\Phi + \Phi')}{2\eta} * F(kLa^+(\Phi + \Phi')) + \\ & \cot\frac{\pi - (\Phi + \Phi')}{2\eta} * F(kLa^-(\Phi + \Phi')) \Bigg\} \end{aligned} \tag{A.2}$$

with

$$F(X) = 2j\sqrt{X}\, e^{jX} \int_{\sqrt{X}}^{\infty} e^{(-j\tau^2)}\, d\tau ,$$

$$a^{\pm}(\Phi \pm \Phi') = 2\cos^2\left(\frac{2\eta\pi N^{\pm} - (\Phi \pm \Phi')}{2}\right),$$

$$k = 2\pi/\lambda ,$$

$N^{\pm}$ are the integers which the expression

$$2\eta\pi N^{\pm} - (\Phi \pm \Phi')$$

comes closest to $\pm \pi$. L is the distance parameter. η is the exterior wedge angle normalized with respect to π.
For plane waves,

$$L = s ,$$

where s is the distance from the observation point to the edge. For an incident cylindrical wave,

$$L = \frac{rr'}{(r + r')}$$

where the cylindrical wave of radius r' is normally incident on the edge and r is the perpendicular distance of the field point from the edge. Φ' is the angle of the incident ray measured from one plane of the edge, Φ is the angle of the diffracted ray measured from the same plane of the edge (cf. Fig. 13).

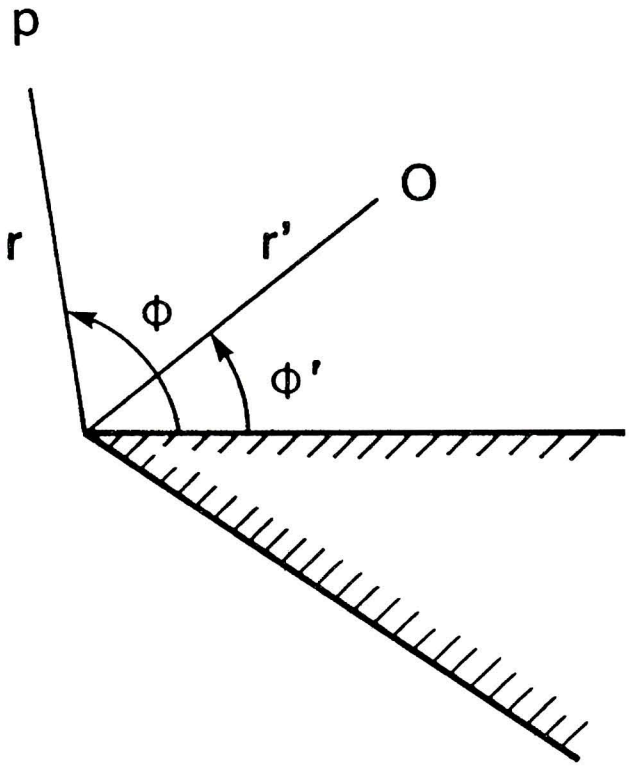

Fig. 13 - Scattering geometry of an edge. ϕ' is the angle measured between the incident ray (OE) and one plane of the edge. ϕ is the angle measured between the diffracted ray (EP) and the same plane of the edge. r' is the radius of the cylindrical wave normally incident on the edge and r is the perpendicular distance from the field point to the edge.

The complex scattering amplitudes for the objects are given by (Ross, 1966):

$$S_{V,H}\, e^{-j\varphi} = \lim_{R_0 \to \infty} \frac{\sqrt{4\pi R_0 f/c}\; b}{E_0\, e^{-j 2\pi R_0 f/c}} \sum u^{d}_{V,H} \qquad (A.3)$$

where the sum accounts for the fields of single and multiple diffracted rays. R_0 is the distance of the antennas to the center of the cuboid. b is the length of the edges, c is the speed of light, E_0 is the field strength of the incident wave. **Single diffraction** occurs at the three visible edges 1,2 and 3 (cf. Fig. 14).

$$u^{d\,\mathrm{single}}{}_{V,H}(R_0) = u^{d1}{}_{V,H}(R_0) + u^{d2}{}_{V,H}(R_0) + u^{d3}{}_{V,H}(R_0) \qquad (A.4)$$

The scalar field of a plane wave incident on an edge is given by:

$$u^{i}{}_{V,H} = E_0\, e^{-jks'} \qquad (A.5)$$

Here s' is the path the wave travels between the point of reference at the edge point (cf. Fig. 13). Substituting A.1 and A.5 in A.4. and approximating $1/\sqrt{s}$ $1/\sqrt{R_0}/2$, and the distance parameter $s_j\, s_{j'}/(s_j + s_{j'}) = R_o/2$

$$u^{d\,\mathrm{single}}{}_{V,H}(R_0) = \frac{e^{-j k R_0}}{\sqrt{R_0}}\; E_0$$

$$\left\{ \begin{array}{l} D_{eh}(\pi/2 + \theta\,,\, \pi/2 + \theta\,,\, k R_0/2) * e^{-j k(-a\sin\theta - d\cos\theta)} + \\ D_{eH}(\theta\,,\, \theta\,,\, k R_0/2) * e^{-j k(-a\sin\theta + d\cos\theta)} + \\ D_{eH}(\pi/2 - \theta\,,\, \pi/2 - \theta\,,\, k R_0) * e^{-j k(a\sin\theta - d\cos\theta)} \end{array} \right\} \qquad (A.6)$$

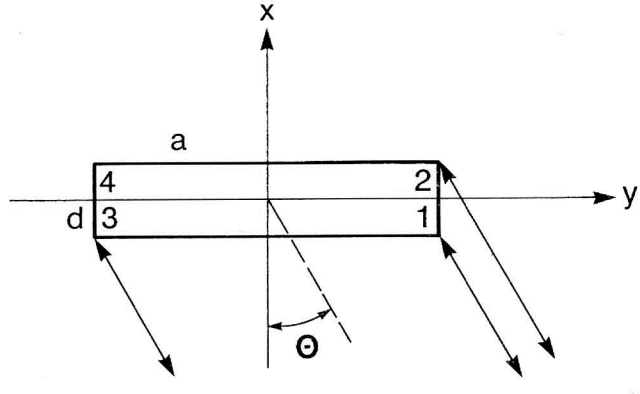

Fig. 14 - UTD-ray paths of fields diffracted once at each of the edges 1,2,3.